

A simple, rigorous benchmark for fully coupled flow–structure interaction algorithms

Tejaswin Parthasarathy^a, Yashraj Bhosale^a, Mattia Gazzola^{a,b,c,*},

^a*Mechanical Sciences and Engineering, University of Illinois at Urbana-Champaign, Urbana, IL 61801, USA*

^b*National Center for Supercomputing Applications, University of Illinois at Urbana-Champaign, Urbana, IL 61801, USA*

^c*Carl R. Woese Institute for Genomic Biology, University of Illinois at Urbana-Champaign, Urbana, IL 61801, USA*

Abstract

We report (semi-)analytical solutions of a benchmark problem for rigorously testing coupled incompressible fluid–elastic solid interaction algorithms. The problem involves a visco-hyperelastic solid material layer sandwiched between two fluid layers, in turn confined by two long planar walls. The walls undergo oscillatory motion which drive a characteristic system response. The governing equations in this setting reduce to one-dimension and admit (semi-)analytical solutions, whose form depends on fluid viscosity and solid elasticity. Using these solutions, we highlight specific parameter settings that serve as rigorous, challenging long-time benchmarks for validating multiphase solvers, in the context of FSI simulations.

1. Introduction

In this report, a benchmark case for testing coupled incompressible fluid–elastic solid interaction algorithms is described. Motivated by the importance of coupled interactions between viscous fluid and visco-hyperelastic solids in biophysical scenarios [1, 2, 3, 4, 5, 6], we provide a well defined, easy to setup benchmark relevant to these settings. More specifically, we extend the previous analysis of Sugiyama et al. [7] to account for solid visco-hyperelasticity and density mismatch in a setup where a viscoelastic solid material layer is sandwiched between two fluid layers which are in turn confined by two long planar walls, whose horizontal oscillations drive a characteristic system response. Here, we consider viscous elastic solids made of neo-Hookean and generalized Mooney–Rivlin materials. The governing equations in this case simplify due to symmetry, giving rise to (semi-)analytic solutions that capture the interplay between the incompressible visco-hyperelastic solid and Newtonian fluid. We carefully detail the steps involved in these solutions so that future investigators may adapt them to establish new benchmarks (for example using different solid constitutive models) or analyze fluid–structure interactions in a simplified setting. These solutions are found to be consistent with classic multiphase Stokes–Couette flow solutions, which are recovered in the limit of zero elasticity [8] with arbitrary fluid–solid viscosity ratios [9, 10]. We then investigate the parametric impact of solid elasticity and fluid viscosity. We conclude by highlighting specific parameter sets that can serve as rigorous, challenging benchmarks for validating multiphase numerical simulation codes.

The work is organized as follows: governing equations are described in Section 2; the problem setup is introduced in Section 3; simplification of the governing equations, solution representations and (semi-)analytical solutions are discussed in Section 4; finally, concluding remarks are provided in Section 5.

2. Governing equations

We begin by presenting the complete set of governing equations and constitutive laws that define the dynamics of multiple rigid/elastic bodies immersed in a viscous fluid.

*Corresponding author

Email address: mgazzola@illinois.edu (Mattia Gazzola)

2.1. Governing equations for solids and fluids

We consider a two-dimensional domain Σ physically occupied by a viscous fluid and elastic solid. We denote with Ω_e & $\partial\Omega_e$ the support and boundaries of the elastic solid, respectively. Denoting $\bar{\Omega} = \bar{\Omega}_e$ to be the region occupied by solid material, the fluid then occupies the region $\Sigma - \bar{\Omega}$.

Linear and angular momentum balance of material volumes in the elastic solid and fluid domains (for Eulerian differential volumes $d\mathbf{x}$), result in the Cauchy momentum equation

$$\frac{\partial \mathbf{v}}{\partial t} + \nabla \cdot (\mathbf{v} \otimes \mathbf{v}) = -\frac{1}{\rho} \nabla p + \frac{1}{\rho} \nabla \cdot \boldsymbol{\sigma}', \quad \mathbf{x} \in \Sigma \quad (1)$$

where $t \in \mathbb{R}^+$ represents time, $\mathbf{v} : \Sigma \times \mathbb{R}^+ \mapsto \mathbb{R}^2$ represents the velocity field, ρ denotes material density, $p : \Sigma \times \mathbb{R}^+ \mapsto \mathbb{R}$ represents the hydrostatic pressure field and $\boldsymbol{\sigma}' : \Sigma \times \mathbb{R}^+ \mapsto \mathbb{R}^2 \otimes \mathbb{R}^2$ is the deviatoric Cauchy stress tensor field. As a convention, the prime symbol ' on a tensor \mathbf{A} denotes it is deviatoric, i.e. $\mathbf{A}' := \mathbf{A} - \frac{1}{2} \text{tr}(\mathbf{A}) \mathbf{I}$, with \mathbf{I} representing the tensor identity and $\text{tr}(\cdot)$ representing the trace operator. We assume that all fields defined above are sufficiently smooth in time and space. Incompressibility of the fluid and elastic domains is kinematically enforced through

$$\nabla \cdot \mathbf{v} \equiv 0, \quad \mathbf{x} \in \Sigma \quad (2)$$

The fluid and elastic solid phases interact exclusively via boundary conditions, imposing continuity in velocities (no-slip) and traction forces at all fluid–elastic solid interfaces

$$\mathbf{v} = \mathbf{v}_f = \mathbf{v}_e, \quad \boldsymbol{\sigma}'_f \cdot \mathbf{n} = \boldsymbol{\sigma}'_e \cdot \mathbf{n}, \quad \mathbf{x} \in \partial\Omega_e \quad (3)$$

where \mathbf{n} denotes the unit outward normal vector at the interface $\partial\Omega_e$. Here \mathbf{v}_f and \mathbf{v}_e correspond to the interfacial velocities in the fluid and the elastic body, respectively, while $\boldsymbol{\sigma}'_f$ and $\boldsymbol{\sigma}'_e$ correspond to the interfacial Cauchy stress tensor in the fluid and the elastic body, respectively.

2.2. Constitutive laws for fluid and elastic solids

To close the above set of equations (Eqs. 1 to 3) and determine the system dynamics, it is necessary to specify the form of internal material stresses, i.e. their constitutive laws. Here, we discuss specific modeling choices for the Cauchy stress tensor $\boldsymbol{\sigma}'$ of Eq. 1, across the different phases.

The fluid is assumed to be Newtonian, isotropic and incompressible with density ρ_f , dynamic viscosity μ_f and kinematic viscosity $\nu_f = \mu_f/\rho_f$. As such, the Cauchy stress is comprised of the purely viscous term

$$\boldsymbol{\sigma}'_f := 2\mu_f \mathbf{D}' \quad (4)$$

where \mathbf{D}' is the strain rate tensor $\frac{1}{2}(\nabla \mathbf{v} + \nabla \mathbf{v}^T)$.

Next, we assume that the elastic solid is isotropic, incompressible, has constant density ρ_s and exhibits both elastic and viscous (or *visco-elastic*) behavior. Then the deviatoric Cauchy stress can be modeled as

$$\boldsymbol{\sigma}'_e := 2\mu_s \mathbf{D}' + \boldsymbol{\sigma}'_{he} \quad (5)$$

where μ_s represents the dynamic viscosity of the solid material (indicative of internal damping effects) and \mathbf{D}' is the strain rate tensor. For convenience, we can also define the kinematic viscosity of the solid $\nu_s = \mu_s/\rho_s$.

The term $\boldsymbol{\sigma}'_{he}$ is the hyperelastic contribution to the solid stress tensor. We describe it here through the generalized Mooney–Rivlin model [7, 11], developed to capture elastomeric and biological tissue material responses. We then consider an elastic solid in a convective coordinate system evolving with time t . At $t = 0$, the solid is in its initial, stress-free configuration. A material point location within the solid is denoted by $\mathbf{X} \in \Omega_e^0 \subset \mathbb{R}^2$. Due to external or internal forces and couples, the solid displaces and distorts in physical space $\mathbf{x} \in \Omega_e(t) \subset \mathbb{R}^2$ for $t > 0$. Phenomenologically, the stress field $\boldsymbol{\sigma}'_{he}$ is a function of the displacement $\mathbf{u} = \mathbf{x} - \mathbf{X}$ (or equivalently strain) of a solid material point, and arises from the strain energy density function W stored in the solid due to deformations. This is equivalent to $\boldsymbol{\sigma}'_{he}$ being only dependent on the deformation gradient $\mathbf{F} := \partial \mathbf{x} / \partial \mathbf{X}$ and not on \mathbf{x} itself (intuitively, purely rigid body motions cause no stress). Galilean invariance dictates that this dependence on \mathbf{F} occurs only through the rotationally-invariant left

$\mathbf{B} := \mathbf{F}\mathbf{F}^T$ or right $\mathbf{C} := \mathbf{F}^T\mathbf{F}$ Cauchy–Green deformation tensors. Without loss of generality, the strain energy density W can then be modeled as a function of \mathbf{C} only

$$W(\mathbf{C}) := c_1(\tilde{\mathbf{I}}_{\mathbf{C}} - 2) + c_2(\tilde{\mathbf{\Pi}}_{\mathbf{C}} - 2) + c_3(\tilde{\mathbf{I}}_{\mathbf{C}} - 2)^2 \quad (6)$$

where c_1, c_2 and c_3 are material constants, and $\tilde{\mathbf{I}}_{\mathbf{C}}$ and $\tilde{\mathbf{\Pi}}_{\mathbf{C}}$ are the reduced invariants of \mathbf{C} defined as

$$\tilde{\mathbf{I}}_{\mathbf{C}} := \frac{\mathbf{I}_{\mathbf{C}}}{\mathbb{III}_{\mathbf{C}}^{1/3}}, \quad \tilde{\mathbf{\Pi}}_{\mathbf{C}} := \frac{\mathbf{\Pi}_{\mathbf{C}}}{\mathbb{III}_{\mathbf{C}}^{2/3}} \quad (7)$$

through the matrix invariants

$$\mathbf{I}_{\mathbf{C}} := \text{tr}(\mathbf{C}), \quad \mathbf{\Pi}_{\mathbf{C}} := \frac{1}{2}(\mathbf{I}_{\mathbf{C}}^2 - \text{tr}(\mathbf{C} \cdot \mathbf{C})), \quad \mathbb{III}_{\mathbf{C}} := \det(\mathbf{C}) \quad (8)$$

with \det representing the determinant operator. By combining Eqs. 6 to 8, we obtain the following expression of hyperelastic stress for an incompressible material

$$\boldsymbol{\sigma}'_{he} = \left(2\mathbf{F} \frac{\partial W(\mathbf{C})}{\partial \mathbf{C}} \mathbf{F}^T \right)' \quad (9)$$

which finally reduces to

$$\boldsymbol{\sigma}'_{he} = \left(2\mathbf{F} \left[c_1 \frac{\partial \tilde{\mathbf{I}}_{\mathbf{C}}}{\partial \mathbf{C}} + c_2 \frac{\partial \tilde{\mathbf{\Pi}}_{\mathbf{C}}}{\partial \mathbf{C}} + c_3(\tilde{\mathbf{I}}_{\mathbf{C}} - 2) \frac{\partial \tilde{\mathbf{I}}_{\mathbf{C}}}{\partial \mathbf{C}} \right] \mathbf{F}^T \right)' = (2c_1\mathbf{B} + 2c_2(\text{tr}(\mathbf{B})\mathbf{B} - \mathbf{B} \cdot \mathbf{B}) + 4c_3(\text{tr}(\mathbf{B}) - 2)\mathbf{B})'. \quad (10)$$

For small deformations, the coefficients $2(c_1 + c_2)$ represent G , the elastic modulus of the solid, and c_3 is loosely related to the bulk modulus (K) of the material. Finally, if we set $c_2 = c_3 = 0$ and $2c_1 = G$ in Eq. 10, we recover the Cauchy stress corresponding to a neo-Hookean material

$$\boldsymbol{\sigma}'_{he} = G\mathbf{B}'. \quad (11)$$

We note that the above linear relation between $\boldsymbol{\sigma}'_{he}$ and \mathbf{B}' does not amount to a linear stress-strain response as in perfectly elastic materials, because $\mathbf{B} := \mathbf{F}\mathbf{F}^T$ contains strain non-linearities which account for Galilean invariance. Indeed, the neo-Hookean model has been developed to capture non-linear stress-strain behaviours, but differently from the generalized Mooney–Rivlin model, it does so to a lesser degree of accuracy and generality. Nonetheless, due to its popularity and for comparison purposes we consider here the neo-Hookean model as well.

With the governing equations established, we now focus on our problem of interest by introducing its setup.

3. Problem setup

A schematic of the setup is shown in Fig. 1. Here, we have a two-dimensional visco-hyperelastic solid sandwiched between two layers of fluid, such that the system is top-down symmetric. The thickness of the solid and each fluid layer is $2L_s$ and L_f respectively. The setup is infinitely long and hence homogeneous in the x direction. The fluid is bounded by two planar walls which present a prescribed sinusoidal oscillatory motion $V_{\text{wall}}(t) := \hat{V}_{\text{wall}} \sin(\omega t) = \text{Im} \left[\hat{V}_{\text{wall}} \exp(i\omega t) \right]$, where hatted quantities denote the Fourier coefficients obtained upon a temporal Fourier transform. The bottom wall oscillates out of phase with the top wall, with phase shift π . We investigate the motion of the coupled solid–fluid system as a result of these wall oscillations. The derivation closely follows [7], but now includes additional terms to account for viscosity and density mismatch in neo-Hookean and generalized Mooney–Rivlin solids.

4. Derivation of analytical and semi-analytical solution

Now we discuss in detail the derivation of the sharp interface (semi-)analytical solutions for this setup.

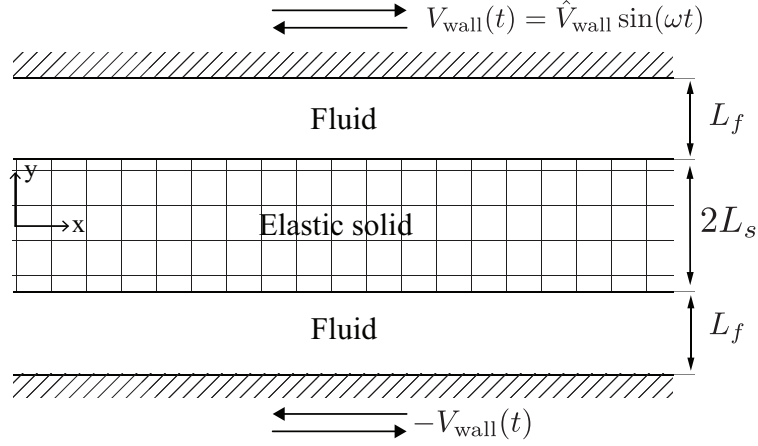


Figure 1: Schematic of the problem setup.

4.1. Simplification of governing equations

We begin by noting that the problem is homogeneous in the x -direction and hence we can omit the x -dependence of any quantity. The problem then reduces to a one-dimensional one, with gradients only along the y -axis, and classical symmetry reductions to the governing Cauchy momentum equation can be adopted. Firstly, the continuity equation (or equivalently the incompressibility condition) of Eq. 2 simplifies to

$$\frac{\partial v_y}{\partial y} \equiv 0$$

A trivial solution to this equation is $v_y(y, t) = c(t)$, where $c(t)$ is an arbitrary quantity. Because of the absence of motion of the wall in the y -direction, $c(t)$ is identically set to 0 to match wall boundary conditions. Then, only the displacement $u(y, t)$, velocity $v(y, t)$ and stresses $\sigma_{xy} = \sigma(y, t)$ in the x direction need to be considered. This simplifies the governing equation Eq. 1 to read as

$$\begin{aligned} \partial_t u &= v, \\ \rho \partial_t v &= \partial_y \sigma. \end{aligned} \quad (12)$$

where all the physical quantities depend on (y, t) . Additionally, the stress can be directly computed from Eqs. 4, 5 and 10 as follows

$$\sigma = \begin{cases} \mu_f \partial_y v & \text{for fluid } (L_s < |y| \leq L_s + L_f) \\ 2c_1 \partial_y u + 4c_3 (\partial_y u)^3 + \mu_s \partial_y v & \text{for solid } (0 \leq |y| < L_s) \end{cases} \quad (13)$$

where we remark that the coefficient c_2 is absent and hence does not contribute to the dynamics. We note that the solid stress expression for a Mooney–Rivlin material with $c_3 = 0$ is linear with respect to the displacement u , while the one with $c_3 \neq 0$ is nonlinear [7]. The velocities and stresses at the interfaces need to be continuous per Eq. 3, thus

$$\begin{aligned} v(\pm L_s^+, t) &= v(\pm L_s^-, t) \\ \mu_f \partial_y v(\pm L_s, t) &= 2c_1 \partial_y u(\pm L_s, t) + 4c_3 (\partial_y u(\pm L_s, t))^3 + \mu_s \partial_y v(\pm L_s, t). \end{aligned} \quad (14)$$

Finally we close the equations above by imposing no-slip boundary conditions at the upper and lower walls at $y = \pm(L_s + L_f)$.

$$v = \begin{cases} \hat{V}_{\text{wall}} \sin \omega t & \text{at } y = L_f + L_s \\ -\hat{V}_{\text{wall}} \sin \omega t & \text{at } y = -(L_f + L_s) \end{cases} \quad (15)$$

4.2. Solution using Fourier series

The solution strategy is to represent $u(y, t)$, $v(y, t)$ as a Fourier sine series in the spatial coordinate y , inject it into the simplified governing equations Eqs. 12 and 13 and match the interfacial conditions in Eq. 14 and boundary conditions in Eq. 15 to obtain closed-form solutions. The choice of a sine series expansion is natural here given the Dirichlet velocity boundary conditions. Given the piecewise definition of stress in Eq. 13 and interfacial condition in Eq. 14 (which indicates that velocities can at most be C^0 continuous), convergence can be poor if a global Fourier series (i.e. for both the solid and fluid domains together) is considered. Hence, we utilize two piecewise Fourier series expansions for the solid $v_s(y, t)$ and fluid $v_f(y, t)$ velocities respectively, with C^0 continuity in velocities and stresses explicitly imposed.

We begin by noting that due to symmetry, Eq. 12 can only admit solutions which are odd functions of y —indeed the equations of motion are invariant upon replacing $u(y, t)$, $v(y, t)$ with $-u(-y, t)$, $-v(-y, t)$. Then one can expand $u(y, t)$, $v(y, t)$ as follows, using the Fourier sine series in only the upper half space $y \geq 0$

$$\begin{aligned} v_f(\tilde{y}, t) &= V_I(t) + \frac{\tilde{y}}{L_f} (V_{\text{wall}}(t) - V_I(t)) + \sum_{k=1}^{\infty} v_{f,k}(t) \sin \frac{\pi k \tilde{y}}{L_f} \\ v_s(y, t) &= \frac{V_I(t)y}{L_s} + \sum_{k=1}^{\infty} v_{s,k}(t) \sin \frac{\pi ky}{L_s} \end{aligned} \quad (16)$$

where $V_I(t)$ is the velocity of the solid–fluid interface at $y = L_s$, $v_{f,k}(t)$ and $v_{s,k}(t)$ are the Fourier expansion coefficients of v_f , v_s respectively, and $\tilde{y} = y - L_s$. This form of expansion satisfies the incompressibility Eq. 2, odd symmetry requirement about $y = 0$, interfacial velocity conditions in Eq. 14 and boundary velocity conditions (Eq. 15) imposed in the setup.

The choice of using piecewise linear functions in the solution, in addition to the Fourier sine series, is natural. Indeed, if we consider the simpler Couette flow case, i.e. only viscous fluid between two parallel plates (at $L = 0$ and $L = L_{\text{wall}}$, with the top wall moving with V_{wall}), the trivial solution lying in the nullspace of the governing continuity and momentum equations (Eq. 12) is $v(y) = V_{\text{wall}}y/L_{\text{wall}}$. The addition of such a trivial solution to the current problem does not affect the Fourier series in any meaningful way (except for a change in the value of coefficients). Formally, the *trivial* solution is a particular solution of the governing linear PDE, arising due to an inhomogeneity caused by a non-zero wall velocity (boundary conditions and forcing terms are interchanged by Duhamel’s principle). One can then view Eq. 16 as a superposition of the particular solution and homogeneous solution to the governing PDE.

From Eq. 16, one can deduce the solid displacement u_s as

$$u_s(y, t) = \frac{U_I(t)y}{L_s} + \sum_{k=1}^{\infty} u_{s,k}(t) \sin \frac{\pi ky}{L_s} \quad (17)$$

with the interface displacement U_I and modal displacement $u_{s,k}$ being

$$\frac{dU_I}{dt} = V_I, \quad \frac{du_{s,k}}{dt} = v_{s,k}. \quad (18)$$

While an equivalent fluid displacement can be defined, it is less meaningful given the typically high strain rates in the fluid phase. Substituting the Fourier-series defined in Eq. 16 into the governing Eq. 12 and utilizing the stress relations of Eq. 13, we rewrite the equations with all terms moved to the LHS as follows

$$\frac{dV_I}{dt} + \frac{\tilde{y}}{L_f} \left(\frac{dV_{\text{wall}}}{dt} - \frac{dV_I}{dt} \right) + \sum_{k=1}^{\infty} \left\{ \frac{dv_{f,k}}{dt} + v_f \left(\frac{\pi k}{L_f} \right)^2 v_{f,k} \right\} \sin \frac{\pi k \tilde{y}}{L_f} = 0 \quad (19)$$

$$\frac{y}{L_s} \frac{dV_I}{dt} + \sum_{k=1}^{\infty} \left\{ \frac{d^2 u_{s,k}}{dt^2} + v_s \left(\frac{\pi k}{L_s} \right)^2 \frac{du_{s,k}}{dt} + \frac{2c_1}{\rho_s} \left(\frac{\pi k}{L_s} \right)^2 u_{s,k} + \frac{\pi k}{\rho_s L_s} \sigma_{\text{NL},k} \right\} \sin \frac{\pi ky}{L_s} = 0 \quad (20)$$

where $v_s = \mu_s/\rho_s$ and $v_f = \mu_f/\rho_f$ are the kinematic viscosities of the solid and fluid phase, respectively. Here σ_{NL} denotes the nonlinear contribution (multiplying c_3) in the solid stress term Eq. 13 with respect to the displacement. The expansion coefficients of σ_{NL} are defined as follows

$$\sigma_{\text{NL}} := 4c_3 \left(\frac{\partial u_s}{\partial y} \right)^3 = \sum_{k=0}^{\infty} \sigma_{\text{NL},k} \cos \frac{\pi ky}{L_s}. \quad (21)$$

We proceed by utilizing the following orthogonality and integral relations for Fourier basis functions, given $k, l \neq 0$

$$\begin{aligned} \text{Orthogonality relations} \quad & \int_0^L \sin \frac{\pi ky}{L} \sin \frac{\pi ly}{L} dy = \frac{L}{2} \delta_{kl} \\ & \int_0^L \cos \frac{\pi ky}{L} \cos \frac{\pi ly}{L} dy = \frac{L}{2} \delta_{kl} \\ \text{Integral relations} \quad & \int_0^L \sin \frac{\pi ky}{L} = \frac{L}{\pi k} [1 - (-1)^k] \\ & \int_0^L \frac{y}{L} \sin \frac{\pi ky}{L} = \frac{L}{\pi k} (-(-1)^k) \end{aligned} \quad (22)$$

where δ_{kl} is the delta function, used in a pointwise sense. Using these relations, the governing equations in physical space (Eqs. 19 and 20) can be equivalently transformed to the modal space by a transformation to Fourier basis

$$\frac{2}{\pi k} \left\{ \frac{dV_I}{dt} - (-1)^k \frac{dV_{\text{wall}}}{dt} \right\} + \frac{dv_{f,k}}{dt} + v_f \left(\frac{\pi k}{L_f} \right)^2 v_{f,k} = 0 \quad (23)$$

$$- \frac{2(-1)^k}{\pi k} \frac{dV_I}{dt} + \frac{d^2 u_{s,k}}{dt^2} + v_s \left(\frac{\pi k}{L_s} \right)^2 \frac{du_{s,k}}{dt} + \frac{2c_1}{\rho_s} \left(\frac{\pi k}{L_s} \right)^2 u_{s,k} + \frac{\pi k}{\rho_s L_s} \sigma_{\text{NL},k} = 0 \quad (24)$$

for $k = 1, \dots, \infty$. The condition for continuity of shear stress at the interface in modal space, upon substituting the Fourier series Eq. 16 into the physical space stress continuity equation Eq. 14 and using the relations of Eq. 22, is

$$\frac{\mu_f (V_{\text{wall}} - V_I)}{L_f} - \frac{2c_1 U_I}{L_s} - \sigma_{\text{NL},0} - \frac{\mu_s V_I}{L_s} \sum_{k=1}^{\infty} \left[\frac{\mu_f \pi k v_{f,k}}{L_f} - (-1)^k \left\{ \frac{2c_1 \pi k u_{s,k}}{L_s} + \frac{\mu_s \pi k}{L_s} \frac{du_{s,k}}{dt} + \sigma_{\text{NL},k} \right\} \right] = 0 \quad (25)$$

Equations 23 to 25 directly relate the modal quantities in the fluid $v_{f,k}$ and solid $u_{s,k}$ via the interfacial quantities U_I, V_I as a function of the physical setup parameters, which we now need to solve. To obtain the modal expansion coefficients $v_{f,k}, u_{s,k}$ and U_I, V_I in the above Eqs. 23 to 25, we truncate the number of modes in the infinite Fourier series to a finite set of terms upto $k = K - 1$. This leads to a truncation error, when compared to the true solution of the above equations, which we minimize by taking K to be large. Here, K is fixed to 1024 unless otherwise indicated.

We now specialize and analyze the above solutions for the cases of neo-Hookean and generalized Mooney–Rivlin solid constitutive materials.

4.2.1. Analytical solution for a neo-Hookean solid

In the case of a neo-Hookean constitutive model, c_3 in Eq. 13 is identically 0. In this case, the governing equations reduce to a set of linear equations given that our setup involves purely shearing motions, apparent from the form of stress in Eq. 13. The modal Eqs. 23 to 25 can then be solved analytically for the expansion coefficients. Considering the sinusoidal form of wall velocity $V_{\text{wall}}(t) = \text{Im} \left[\hat{V}_{\text{wall}} \exp(i\omega t) \right]$ one can expect a similar form for the other physical quantities given the symmetry of the setup

$$\begin{aligned} V_I(t) &= \text{Im} \left[\hat{V}_I \exp(i\omega t) \right] \\ v_{f,k}(t) &= \text{Im} \left[\hat{v}_{f,k} \exp(i\omega t) \right] \\ u_{s,k}(t) &= \text{Im} \left[\hat{u}_{s,k} \exp(i\omega t) \right]. \end{aligned} \quad (26)$$

An immediate implication is that

$$\begin{aligned}
U_I(t) &= \text{Im} \left[\frac{\hat{V}_I}{i\omega} \exp(i\omega t) \right] \\
v_{s,k}(t) &= \frac{du_{s,k}}{dt} = \text{Im} [i\omega \hat{u}_{s,k} \exp(i\omega t)] \\
\frac{d^2 u_{s,k}}{dt^2} &= \text{Im} [-\omega^2 \hat{u}_{s,k} \exp(i\omega t)].
\end{aligned} \tag{27}$$

Substitution of the temporal transformed quantities from Eqs. 26 and 27 in the momentum ODEs (Eqs. 23 and 24) reduces them to algebraic equations which can then be solved. Upon algebraic manipulation and taking into account the modal stress balance (Eq. 25), we finally obtain

$$\begin{aligned}
\hat{v}_{f,k} &= \frac{\{(-1)^k \hat{V}_{\text{wall}} - \hat{V}_I\} \alpha_k}{\pi k} \\
\hat{u}_{s,k} &= -\frac{i(-1)^k \hat{V}_I \beta_k}{\pi \omega k} \\
\hat{V}_I &= \frac{\frac{\mu_f \hat{V}_{\text{wall}}}{L_f} \left(1 + \sum_{k=1}^{K-1} (-1)^k \alpha_k\right)}{\frac{\mu_f}{L_f} \left(1 + \sum_{k=1}^{K-1} \alpha_k\right) + \left(\frac{\mu_s}{L_s} + \frac{2c_1}{i\omega L_s}\right) \left(1 + \sum_{k=1}^{K-1} \beta_k\right)}
\end{aligned} \tag{28}$$

where

$$\begin{aligned}
\alpha_k &= \frac{2i\omega}{\frac{\pi^2 k^2}{L_f^2} \nu_f + i\omega} \\
\beta_k &= \frac{2i\omega}{\frac{\pi^2 k^2}{L_s^2} \left[\frac{2c_1}{i\omega \rho_s} + \nu_s\right] + i\omega}.
\end{aligned} \tag{29}$$

In general, the proposed system can be conveniently characterized through the following parameters

- Length scale $L := 2(L_s + L_f)$
- Shear rate $\dot{\gamma} := 2\hat{V}_{\text{wall}}/L$
- Reynolds number $Re := \gamma \dot{L}_f^2 / \nu_f$
- Ericksen number $Er := \mu_f \dot{\gamma} / 2c_1$
- Viscosity ratios $\nu := \nu_s / \nu_f$

A typical temporal non-dimensional velocity profile in the upper half plane obtained directly from Eqs. 28 and 29 is shown in Fig. 2, for a system characterized by $Re = 2$, $Er = 1$, $\nu = 0.1$. Detailed parameters can be found in the image caption. Additionally, we note that

- In the limit of $\mu_s = 0$, i.e. a purely elastic solid, we recover the solution given in Sugiyama et al. [7] (typographical errors in that work exempted)

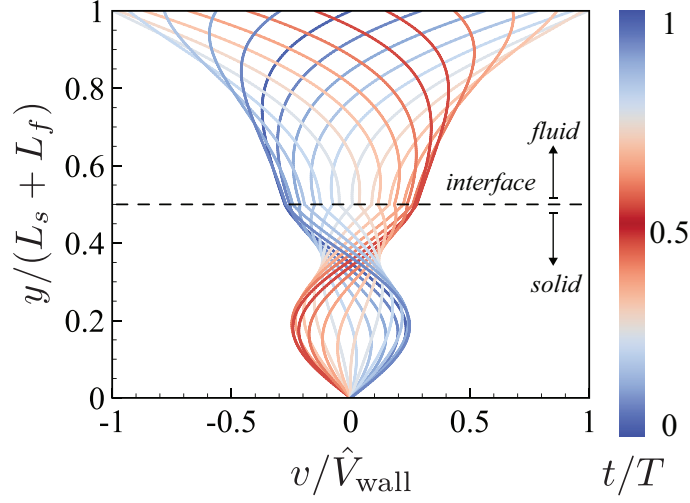


Figure 2: Non-dimensional velocity profile versus y in the case involving an elastic solid with a neo-Hookean constitutive model, shown only in the upper half plane. This system is characterized by $Re = 2, Er = 1, \nu = 0.1$. The parameters used in this case are $L_s = L_f = L/4, \rho_f = \rho_s = 1, \mu_f = 0.02, \mu_s = 0.1\mu_f, c_1 = 0.01, c_3 = 0, \hat{V}_{\text{wall}} = 0.4, \omega = \pi$. Colors represent t/T .

- In the limit of $c_1 = 0$ and $\mu_s = \mu_f = \mu$ and $\rho_s = \rho_f = \rho$, i.e. when the entire domain is occupied by a fluid of kinematic viscosity ν , we recover the Stokes–Couette flow solution [8] below

$$v(y, t) = \hat{V}_{\text{wall}} \text{Im} \left[\frac{\sin(ky)}{\sin(k(L_s + L_f))} \exp(i\omega t) \right]; \quad k = \frac{1-i}{\sqrt{2}} \sqrt{\frac{\omega}{\nu}}$$

valid throughout the domain. Upon overlaying the velocity profiles in Fig. 3, they compare well for a representative case with $Re = 2$ and $\nu = 1$.

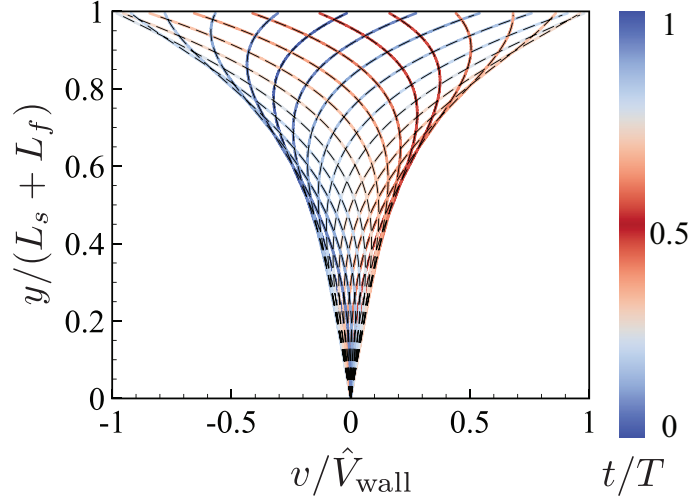


Figure 3: Non-dimensional velocity profile versus y in the case involving the solid replaced by the surrounding, identical viscous fluid, shown only for the upper half plane. We compare our results with the reference Stokes–Couette solution [8], shown in black dashed lines, and find them in agreement with each other. This system is characterized by $Re = 2, \nu = 0.1$. The parameters used in this case are $L_s = L_f = L/4, \rho_f = \rho_s = 1, \mu_f = 0.02, \mu_s = \mu_f, c_1 = 0.0, c_3 = 0, \hat{V}_{\text{wall}} = 0.4, \omega = \pi$. Colors represent t/T .

- Finally, in the limit of $c_1 = 0$, but now with $\mu_s \neq \mu_f$ or $\rho_s \neq \rho_f$, i.e. with the domain occupied by two different fluids, we recover the multi-phase Stokes–Couette flow between two immiscible liquids, which has established

analytical solutions [9, 10]. We showcase our solutions and compare it with these established solutions, for a representative case with $Re = 2$ and $\nu = \nu_1/\nu_2 = 0.1$ and $\nu = 10$ in Fig. 4a,b respectively. We note that this setup is especially suited as an initial/preliminary benchmark for two-fluid simulations since the interface does not deform (due to symmetry) and so curvature effects (such as those encountered while modeling surface tension effects) are identically absent. Hence only the terms contributing to interfacial stress jump are tested.

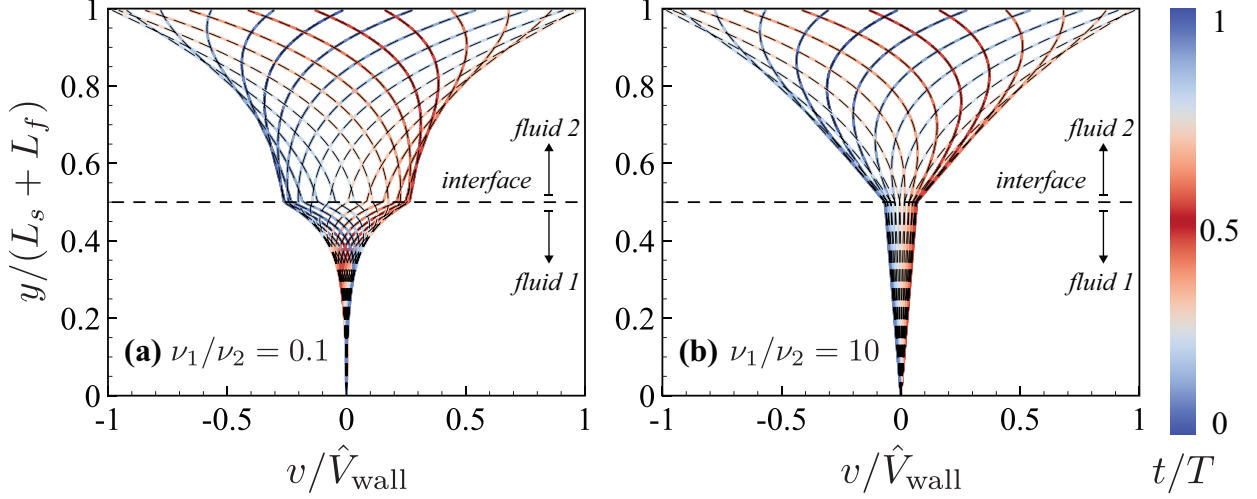


Figure 4: Non-dimensional velocity profile versus y in the case involving the solid replaced by an equivalent viscous fluid, shown only for the upper half plane, for viscosity ratios $\nu = \nu_1/\nu_2 = (a) 0.1$ and $(b) 10$. We compare our results with the reference two-fluid Stokes–Couette solution [9, 10], shown in black dashed lines, and find them in agreement with each other. The other parameters used in this case are $L_s = L_f = L/4$, $\rho_f = \rho_s = 1$, $\mu_f = 0.02$, $c_1 = 0$, $c_3 = 0$, $\hat{V}_{\text{wall}} = 0.4$, $\omega = \pi$. Colors represent t/T .

We have thus provided analytical solutions for the dynamics of a viscoelastic neo-Hookean solid immersed in a viscous fluid. We have extended the previous work of Sugiyama et al. [7] to account for arbitrary solid densities and viscosities. As a special limiting case, we recover the original solution of Sugiyama et al. [7] for a density-matched solid with zero viscosity. Additionally we recover previous analytical solutions of single [8] and multi-fluid [9, 10] Stokes–Couette flows in the limit of zero solid elasticity. The solution exhibits a wide range of behavior in these cases (Figs. 2 to 4) and is as a useful benchmark to validate strongly coupled solid–fluid interaction solvers.

4.2.2. Numerical solution for a generalized Mooney–Rivlin solid

In the case of a generalized Mooney–Rivlin solid, characterized by $c_3 \neq 0$, the hyperelastic stress is proportional to the cubic power of strain in Eq. 13 which signifies a non-linear response to deformations. In this case a semi-analytical solution, to be evaluated numerically, can be derived. First, we calculate the modal expansion coefficients of the nonlinear stresses $\sigma_{\text{NL},k}$ in the governing Eq. 24. For this calculation we employ a Fourier pseudospectral collocation scheme [7]. The following cosine orthogonality relation is useful in this case

$$\int_0^L \cos \frac{\pi ky}{L} \cos \frac{\pi ly}{L} dy = \frac{L}{2} \delta_{kl} (1 + \delta_{k0}) \quad (30)$$

Then upon transforming Eq. 21 into the Fourier cosine bases and using Eq. 30, we obtain the following expression for $\sigma_{\text{NL},k}$

$$\sigma_{\text{NL},k} \approx \frac{8c_3}{K(1 + \delta_{k0})} \sum_{j=0}^{K-1} \left\{ \frac{U_I}{L_s} + \sum_{l=1}^{K-1} \frac{\pi l u_{s,l}}{L_s} \cos \frac{\pi l (j + \frac{1}{2})}{K} \right\}^3 \cos \frac{\pi k (j + \frac{1}{2})}{K} \quad (31)$$

which is approximate, with errors incurred from truncation (discussed before in Section 4.2) and our choice of collocated quadrature which is associated with spatial discretization and sampling of the nonlinear term $(\partial u_s/\partial y)^3$ at a finite set of points $x_j = (j + \frac{1}{2})\Delta x$, with $\Delta x = L_s/K$.

Next, we employ a numerical time integration scheme to evolve the non-linear Eqs. 23 and 24. We use a second order constant timestep method comprised of mixed Crank-Nicolson (implicit, for stability in the viscous updates) and explicit Nyström (midpoint rule) for the higher order time derivatives [12]. The n^{th} time level at $t = n\Delta t$ is denoted by a superscript (n) . First, the prescribed wall velocity is

$$V_{\text{wall}}^{(n+1)} := V_{\text{wall}}((n+1)(\Delta t)) = \text{Im} \left[\hat{V}_{\text{wall}} \exp(i\omega((n+1)\Delta t)) \right]. \quad (32)$$

For the U_I update, which proceeds independently of the governing Eqs. 23 and 24 we use the Crank-Nicolson scheme [12], shown below

$$U_I^{(n+1)} \approx U_I^{(n)} + \frac{\Delta t}{2} (V_I^{(n+1)} + V_I^{(n)}) + \mathcal{O}(\Delta t^2) \quad (33)$$

We then turn our attention to the modal fluid momentum Eq. 23. For updating the fluid velocity modes with the action of the viscous terms, we once again utilize the Crank-Nicolson discretization at time level n

$$\frac{2}{\pi k} \left\{ \frac{V_I^{(n+1)} - V_I^{(n)}}{\Delta t} - (-1)^k \frac{V_{\text{wall}}^{(n+1)} - V_{\text{wall}}^{(n)}}{\Delta t} \right\} + \frac{v_{f,k}^{(n+1)} - v_{f,k}^{(n)}}{\Delta t} = -\nu_f \left(\frac{\pi k}{L_f} \right)^2 \frac{1}{2} (v_{f,k}^{(n+1)} + v_{f,k}^{(n)}) + \mathcal{O}(\Delta t^2) \quad (34)$$

where we note that both wall and interface velocities on the LHS are discretized consistently with $v_{f,k}$. Rearranging the terms in the equation above results in the following fluid mode update, accurate up to second order in Δt

$$v_{f,k}^{(n+1)} = \frac{E_{f,k}}{\zeta_{f,k}} \quad (35)$$

where

$$E_{f,k} = (2 - \zeta_{f,k}) v_{f,k}^{(n)} - \frac{2 \{ V_I^{(n+1)} - V_I^{(n)} - (-1)^k \delta V_{\text{wall}} \}}{\pi k} \quad (36)$$

$$\zeta_{f,k} = 1 + \nu_f \frac{\Delta t}{2} \left(\frac{\pi k}{L_f} \right)^2 \quad (37)$$

with

$$\delta V_{\text{wall}} = V_{\text{wall}}^{(n+1)} - V_{\text{wall}}^{(n)}. \quad (38)$$

Next, we focus on the modal solid momentum Eq. 24. Here, for updating solid displacements, we utilize the following explicit Nyström (midpoint rule) discretizations at the n^{th} time step

$$\begin{aligned} \left(\frac{dV_I}{dt} \right)^{(n)} &\approx \frac{V_I^{(n+1)} - V_I^{(n-1)}}{2\Delta t} + \mathcal{O}(\Delta t^2) \\ \left(\frac{du_{s,k}}{dt} \right)^{(n)} &\approx \frac{u_{s,k}^{(n+1)} - u_{s,k}^{(n-1)}}{2\Delta t} + \mathcal{O}(\Delta t^2) \\ \left(\frac{d^2 u_{s,k}}{dt^2} \right)^{(n)} &\approx \frac{u_{s,k}^{(n+1)} - 2u_{s,k}^{(n)} + u_{s,k}^{(n-1)}}{(\Delta t)^2} + \mathcal{O}(\Delta t^2) \end{aligned}$$

Upon substituting these discretizations in Eq. 24, we arrive at

$$\begin{aligned} & - \frac{2(-1)^k}{\pi k} \frac{V_I^{(n+1)} - V_I^{(n-1)}}{2\Delta t} + \frac{u_{s,k}^{(n+1)} - 2u_{s,k}^{(n)} + u_{s,k}^{(n-1)}}{(\Delta t)^2} + \\ & \nu_s \left(\frac{\pi k}{L_s} \right)^2 \frac{u_{s,k}^{(n+1)} - u_{s,k}^{(n-1)}}{2\Delta t} + \frac{2c_1}{\rho_s} \left(\frac{\pi k}{L_s} \right)^2 u_{s,k}^{(n)} + \frac{\pi k}{\rho_s L_s} \sigma_{\text{NL},k}^{(n)} + \mathcal{O}(\Delta t^2) = 0 \end{aligned} \quad (39)$$

which upon algebraic manipulation leads to a second order temporally accurate solid displacement mode update

$$u_{s,k}^{(n+1)} = \frac{1}{\zeta_{s,k}} \left[\frac{(-1)^k \Delta t (V_I^{(n+1)} - V_I^{(n-1)})}{\pi k} + 2u_{s,k}^{(n)} - (2 - \zeta_{s,k}) u_{s,k}^{(n-1)} - (\Delta t)^2 \left(\frac{2c_1}{\rho_s} \left(\frac{\pi k}{L_s} \right)^2 u_{s,k}^{(n)} + \frac{\pi k}{\rho_s L_s} \sigma_{\text{NL},k}^{(n)} \right) \right] \quad (40)$$

with

$$\zeta_{s,k} = 1 + \nu_s \frac{\Delta t}{2} \left(\frac{\pi k}{L_s} \right)^2. \quad (41)$$

Finally, we get a closed form for all the expressions by invoking the modal stress balance Eq. 25 at the $(n+1)$ th time level below. Our choice of discretization at the $(n+1)$ th step, rather than at the n th step, ensures that the updates to the solid Eq. 40 and fluid Eq. 35 modes are consistent with each other.

$$\begin{aligned} & \left(\underbrace{\frac{\mu_f (V_{\text{wall}} - V_I)}{L_f} - \frac{2c_1 U_I}{L_s} - \sigma_{\text{NL},0} - \frac{\mu_s V_I}{L_s}}_{\text{I}} \right)^{(n+1)} + \\ & \left(\underbrace{\sum_{k=1}^{\infty} \left[\frac{\mu_f \pi k v_{f,k}}{L_f} - (-1)^k \left\{ \frac{2c_1 \pi k u_{s,k}}{L_s} + \frac{\mu_s \pi k}{L_s} \frac{du_{s,k}}{dt} + \sigma_{\text{NL},k} \right\} \right]}_{\text{II}} \right)^{(n+1)} = 0 \end{aligned} \quad (42)$$

In the above Eq. 42, we first describe the time discretization of the first term, denoted by the under-brace I. For this term, the nonlinear contribution σ_{NL} needs to be extrapolated forward in time to the $(n+1)$ th step. To achieve this, we utilize the second-order accurate extrapolation EXT2 [12] scheme whose formula is shown below.

$$\sigma_{\text{NL},0}^{(n+1)} \approx 2\sigma_{\text{NL},0}^{(n)} - \sigma_{\text{NL},0}^{(n-1)} + \mathcal{O}(\Delta t^2) \quad (43)$$

This discretization is physically motivated, as the nonlinear terms govern the evolution of *slow* elastic wave time scales (compared to *fast* diffusive time scales), ensuring that errors associated with extrapolation are minimal. Upon substituting the discretizations of Eqs. 33 and 43 in the term I discussed above, we arrive at

$$\text{I} \approx \frac{\mu_f (V_{\text{wall}}^{(n+1)} - V_I^{(n+1)})}{L_f} - \frac{2c_1}{L_s} \left(U_I^{(n)} + \frac{\Delta t}{2} (V_I^{(n+1)} + V_I^{(n)}) \right) - (2\sigma_{\text{NL},0}^{(n)} - \sigma_{\text{NL},0}^{(n-1)}) - \frac{\mu_s V_I^{(n+1)}}{L_s} + \mathcal{O}(\Delta t^2) \quad (44)$$

Next, we discuss the time-discretization of the second term, denoted by the under-brace II in Eq. 42. The following formulae are used for discretizing the terms in this case

$$\left(\frac{du_{s,k}}{dt} \right)^{(n+1)} \approx \frac{3u_{s,k}^{(n+1)} - 4u_{s,k}^{(n)} + u_{s,k}^{(n-1)}}{2\Delta t} + \mathcal{O}(\Delta t^2)$$

$$\sigma_{\text{NL},k}^{(n+1)} \approx 2\sigma_{\text{NL},k}^{(n)} - \sigma_{\text{NL},k}^{(n-1)} + \mathcal{O}(\Delta t^2)$$

where the first discretization stems from the family of backward-difference formulae (BDF) [12] and the second discretization is similar to Eq. 43. Upon substituting these discretizations, the second term II now reads

$$\text{II} \approx \sum_{k=1}^{\infty} \left[\frac{\mu_f \pi k v_{f,k}^{(n+1)}}{L_f} - (-1)^k \left\{ \frac{2c_1 \pi k u_{s,k}^{(n+1)}}{L_s} + \frac{\mu_s \pi k}{L_s} \left(\frac{3u_{s,k}^{(n+1)} - 4u_{s,k}^{(n)} + u_{s,k}^{(n-1)}}{2\Delta t} \right) + 2\sigma_{\text{NL},k}^{(n)} - \sigma_{\text{NL},k}^{(n-1)} \right\} \right] + \mathcal{O}(\Delta t^2) \quad (45)$$

Now the terms at the $(n+1)$ th step involving $v_{f,k}$, $u_{s,k}$ here can be directly substituted with the previously derived modal update expressions (Eqs. 35 and 40). Following Eq. 42 we set I + II = 0, using their discretized versions in Eqs. 44 and 45. After standard (but tedious) algebraic manipulations, we finally arrive at the update equation for the interface velocity $V_I^{(n+1)}$

$$V_I^{(n+1)} = \frac{E_I}{\frac{\mu_f}{L_f} \left(1 + 2 \sum_{k=1}^{K-1} \frac{1}{\zeta_{f,k}} \right) + \frac{\mu_s}{L_s} \left(1 + \frac{3}{2} \sum_{k=1}^{K-1} \frac{1}{\zeta_{s,k}} \right) + \frac{c_1 \Delta t}{L_s} \left(1 + 2 \sum_{k=1}^{K-1} \frac{1}{\zeta_{s,k}} \right)} \quad (46)$$

where

$$\begin{aligned}
E_I &= \frac{\mu_f V_{\text{wall}}^{(n+1)}}{L_f} - \frac{c_1}{L_s} \left\{ 2U_I^{(n)} + (\Delta t)V_I^{(n)} \right\} - 2\sigma_{\text{NL},0}^{(n)} + \sigma_{\text{NL},0}^{(n-1)} \\
&+ \sum_{k=1}^{K-1} \frac{\mu_f}{\zeta_{f,k} L_f} \left[\pi k (2 - \zeta_{f,k}) v_{f,k}^n + 2 \left(V_I^{(n)} + (-1)^k \delta V_{\text{wall}} \right) \right] \\
&+ \sum_{k=1}^{K-1} \frac{2c_1}{\zeta_{s,k} L_s} \left[V_I^{(n-1)} \Delta t + (-1)^k \pi k \left(\gamma_k u_{s,k}^{(n)} + (2 - \zeta_{s,k}) u_{s,k}^{(n-1)} \right) \right] \\
&+ \sum_{k=1}^{K-1} \frac{\mu_s}{\zeta_{s,k} L_s \Delta t} \left[\frac{3}{2} V_I^{(n-1)} \Delta t + (-1)^k \pi k \left(\left\{ \frac{3}{2} \gamma_k + 2\zeta_{s,k} \right\} u_{s,k}^{(n)} + \left\{ \frac{3}{2} (2 - \zeta_{s,k}) - \frac{1}{2} \zeta_{s,k} \right\} u_{s,k}^{(n-1)} \right) \right] \\
&+ \sum_{k=1}^{K-1} (-1)^k \left(\left\{ \frac{\gamma_k + 2}{\zeta_{s,k}} + \frac{3}{2} \frac{v_s(\Delta t)}{\zeta_{s,k}} \left(\frac{\pi k}{L_s} \right)^2 \right\} \sigma_{\text{NL},k}^{(n)} + \sigma_{\text{NL},k}^{(n-1)} \right) \\
\gamma_k &= \frac{2c_1}{\rho_s} \left(\frac{\pi k \Delta t}{L_s} \right)^2 - 2
\end{aligned} \tag{47}$$

$$\gamma_k = \frac{2c_1}{\rho_s} \left(\frac{\pi k \Delta t}{L_s} \right)^2 - 2 \tag{48}$$

To summarize, the final formulae used are reproduced below for convenience

$$\begin{aligned}
U_I^{(n+1)} &= U_I^{(n)} + \frac{\Delta t}{2} \left(V_I^{(n+1)} + V_I^{(n)} \right) \\
v_{f,k}^{(n+1)} &= \frac{E_{f,k}}{\zeta_{f,k}} \\
u_{s,k}^{(n+1)} &= \frac{1}{\zeta_{s,k}} \left[\frac{(-1)^k \Delta t \left(V_I^{(n+1)} - V_I^{(n-1)} \right)}{\pi k} + 2u_{s,k}^{(n)} - (2 - \zeta_{s,k}) u_{s,k}^{(n-1)} - \right. \\
&\quad \left. (\Delta t)^2 \left(\frac{2c_1}{\rho_s} \left(\frac{\pi k}{L_s} \right)^2 u_{s,k}^{(n)} + \frac{\pi k}{\rho_s L_s} \sigma_{\text{NL},k}^{(n)} \right) \right] \\
V_I^{(n+1)} &= \frac{E_I}{\frac{\mu_f}{L_f} \left(1 + 2 \sum_{k=1}^{K-1} \frac{1}{\zeta_{f,k}} \right) + \frac{\mu_s}{L_s} \left(1 + \frac{3}{2} \sum_{k=1}^{K-1} \frac{1}{\zeta_{s,k}} \right) + \frac{c_1 \Delta t}{L_s} \left(1 + 2 \sum_{k=1}^{K-1} \frac{1}{\zeta_{s,k}} \right)}
\end{aligned}$$

with

$$\begin{aligned}
\zeta_{s,k} &= 1 + v_s \frac{\Delta t}{2} \left(\frac{\pi k}{L_s} \right)^2 \\
\zeta_{f,k} &= 1 + v_f \frac{\Delta t}{2} \left(\frac{\pi k}{L_f} \right)^2 \\
\delta V_{\text{wall}} &= V_{\text{wall}}^{(n+1)} - V_{\text{wall}}^{(n)} \\
\gamma_k &= \frac{2c_1}{\rho_s} \left(\frac{\pi k \Delta t}{L_s} \right)^2 - 2 \\
E_{f,k} &= (2 - \zeta_{f,k}) v_{f,k}^{(n)} - \frac{2 \left\{ V_I^{(n+1)} - V_I^{(n)} - (-1)^k \delta V_{\text{wall}} \right\}}{\pi k}
\end{aligned}$$

A typical temporal non-dimensional velocity profile in the upper half plane obtained by solving the above equations is shown in Fig. 5. This case is characterized by $Re = 2$, $Er = 1$, $\nu = 0.1$. We define an additional parameter indicating the extent of solid non-linearity $c = \frac{c_3}{c_1}$, which is set to 4, chosen for demonstrating the non-linear behavior of the system in this case. This non-linearity is clearly visible in the solid phase, where the solution now displays sharp ‘‘bends’’ in its profile. Additional parameters can be found in the image caption.

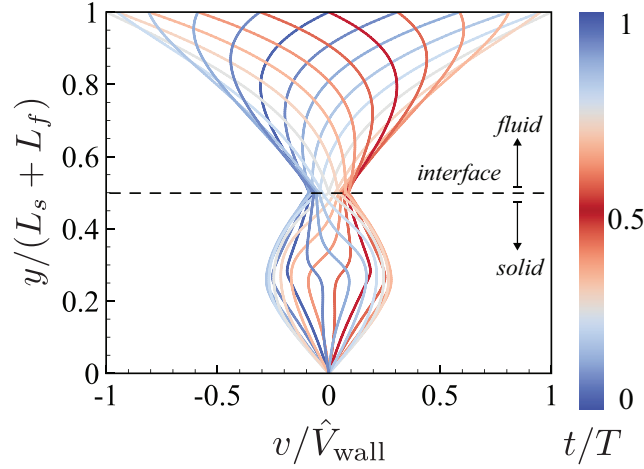


Figure 5: Non-dimensional velocity profile versus y in the case involving an elastic solid with a generalized Mooney–Rivlin model, shown only in the upper half plane. This system is characterized by $Re = 2$, $Er = 1$, $\nu = 0.1$, $c = c_3/c_1 = 4$. The parameters used in this case are $L_s = L_f = L/4$, $\rho_f = \rho_s = 1$, $\mu_f = 0.02$, $\mu_s = 0.1\mu_f$, $c_1 = 0.01$, $c_3 = 0.04$, $\hat{V}_{\text{wall}} = 0.4$, $\omega = \pi$. Colors represent t/T .

5. Conclusion

In conclusion, we have presented solutions for a setup involving parallel viscoelastic solid–fluid layers sandwiched between oscillating walls. We are motivated by the importance of coupled interactions between viscous fluid and visco-hyperelastic solids in many biophysical scenarios, and the consequent need for rigorous benchmarks. Here, we extend the previous analysis of Sugiyama et al. [7] to account for solid visco-hyperelasticity and density mismatch. For a sandwiched viscous neo-Hookean solid, the governing equations simplify to result in an analytically tractable problem for which we derive solutions based on partitioned Fourier-series expansions. We recover the classical Stokes–Couette solution for single and multiple, immiscible fluids at the zero elasticity limit of the proposed solution. For a solid made of a generalized Mooney–Rivlin material with internal viscosity, the simplified equations retain characteristic non-linearity. We then solve the derived semi-analytic solutions numerically using a Fourier-pseudospectral scheme. For all cases we report representative velocity profiles to demonstrate the effect of parametric changes in solid elasticity and fluid viscosity. Given its neat definition, relative simplicity and the wide range of system responses triggered by parametric changes, we propose the above setup as a benchmark problem to rigorously test coupled incompressible fluid–elastic solid interaction algorithms.

References

- [1] S. Alben, M. Shelley, J. Zhang, Drag reduction through self-similar bending of a flexible body, *Nature* 420 (2002) 479–481.
- [2] C. Pozrikidis, *Modeling and simulation of capsules and biological cells*, CRC Press, 2003.
- [3] E. D. Tytell, M. C. Leftwich, C.-Y. Hsu, B. E. Griffith, A. H. Cohen, A. J. Smits, C. Hamlet, L. J. Fauci, Role of body stiffness in undulatory swimming: insights from robotic and computational models, *Physical Review Fluids* 1 (2016) 073202.
- [4] M. Gazzola, M. Argentina, L. Mahadevan, Gait and speed selection in slender inertial swimmers, *Proceedings of the National Academy of Sciences* 112 (2015) 3874–3879.
- [5] X. Zhang, F. K. Chan, T. Parthasarathy, M. Gazzola, Modeling and simulation of complex dynamic musculoskeletal architectures, *Nature communications* 10 (2019) 1–12.
- [6] Y. Bhosale, E. Esmaili, K. Bhar, S. Jung, Bending, twisting and flapping leaf upon raindrop impact, *Bioinspiration & Biomimetics* 15 (2020) 036007.
- [7] K. Sugiyama, S. Ii, S. Takeuchi, S. Takagi, Y. Matsumoto, A full eulerian finite difference approach for solving fluid–structure coupling problems, *Journal of Computational Physics* 230 (2011) 596–627.
- [8] L. Landau, E. Lifshitz, *Theoretical physics*, vol. 6, fluid mechanics, 1987.
- [9] W.-G. Sim, Stratified steady and unsteady two-phase flows between two parallel plates, *Journal of mechanical science and technology* 20 (2006) 125.
- [10] S. Leclaire, N. Pellerin, M. Reggio, J. Trépanier, Unsteady immiscible multiphase flow validation of a multiple-relaxation-time lattice boltzmann method, *Journal of Physics A: Mathematical and Theoretical* 47 (2014) 105501.
- [11] A. F. Bower, *Applied mechanics of solids*, CRC press, 2009.
- [12] E. Hairer, S. P. Nørsett, G. Wanner, *Solving ordinary differential equations I, Nonstiff problems*, Springer-Vlg, 1991.